Icarus **160**, 289–299 (2002)
doi:10.1006/icar.2002.6975

A Global Solution for the Gravity Field, Rotation, Landmarks, and Ephemeris of Eros

Alexander S. Konopliv, James K. Miller, William M. Owen, Donald K. Yeomans, and Jon D. Giorgini

MS 301-125J, Jet Propulsion Laboratory, California Institute of Technology, Pasadena, California 91109
E-mail: alex.konopliv@jpl.nasa.gov

and

Romain Garmier and Jean-Pierre Barriot

Observatoire Midi-Pyrénées, 14 Ave. E. Belin, 31400 Toulouse, France

Received May 20, 2002; revised August 8, 2002

As part of the *NEAR* Radio Science investigation, a global solution that includes both spherical and ellipsoidal harmonic gravity fields of Eros, Eros pole and rotation rate, Eros ephemeris, and landmark positions from the optical data was generated. This solution uses the entire one-year in orbit collection of X-band radiometric tracking (Doppler and range) from the Deep Space Network and landmark tracking observations generated from the *NEAR* spacecraft images of Eros. When compared to a constant density shape model, the gravity field shows a nearly homogeneous Eros. The Eros landmark solutions are in good agreement with the Eros shape model, and they reduce the center-of-mass and center-of-figure offset in the z direction to 13 m. Most of the *NEAR* spacecraft orbits are determined in all directions to an accuracy of several meters. The solution for the ephemeris of Eros constrains the mass of Vesta to 18.2 ± 0.4 km^3/s^2 and reduces the uncertainty in the Earth–Moon mass ratio.

Key Words: **asteroids, Eros; asteroids, Vesta; asteroids, rotation; surfaces, asteroids.**

INTRODUCTION

The *NEAR–Shoemaker* spacecraft was in orbit around 433 Eros for one year from orbit insertion on February 14, 2000 to landing on the asteroid surface on February 12, 2001. The science objectives included the measurement of the gravity field of Eros from Doppler tracking and the determination of the asteroid shape with the *NEAR* Laser Rangefinder (NLR). The comparison of the gravity and shape indicates the uniformity of the asteroid's mass distribution. The spherical harmonic gravity fields of Eros from the joint effort of the Radio Science investigation and the JPL Navigation Team have been previously presented by Yeomans *et al*. (2000) and Miller *et al*. (2002), where Miller *et al*. (2002) showed results using two independent software sets (Orbit Determination Program or ODP of Moyer (1971) and PCODP). The PCODP software was developed by Miller specifically for missions to small bodies and, in particular, for *NEAR* navigation. This paper provides an updated solution to the ODP solution in Miller *et al*. (2002). Whereas the previous ODP solution was based only upon a subset of radiometric data, this new solution uses the entire radiometric and optical landmark data set. This solution has been archived in the Planetary Data System (PDS) as JPL gravity solution NEAR15A (or file JGE15A01.SHA). The ellipsoidal gravity solution for Eros is also based on the same complete data set and has been previously presented by Garmier *et al*. (2002). It provides similar scientific conclusions on the homogeneity of Eros as to the spherical harmonics. This paper provides the processing details on how this ellipsoidal solution was generated.

The previous conclusions on the uniformity of Eros were based upon a shape model developed by the Navigation Team of Miller *et al*. (2002) or Miller's shape model 101. This model contains the same long wavelength features as the model developed by the NLR team of Zuber *et al*. (2000), and both show nearly the same results when compared to the gravity field. So the scientific conclusions for the gravity are unchanged. However, the landmarks contain the short-wavelength information on the shape model, and an accurate high-resolution model is needed to evaluate the landmark solutions. The shape models developed by the Navigation and Radio Science teams are not accurate enough to fully assess the landmark solutions. However, when comparing the landmarks to the high-resolution 180th spherical harmonic degree shape model of the NLR team (Zuber *et al*. 2000), the results are very good. So we will use this model to present all the results requiring a shape model.

The initial orbit for *NEAR* was nearly circular with a radius of about 350 km and an inclination of 35° to the equator of Eros. The orbit of *NEAR* was progressively lowered as the rotation and gravity field of Eros became better known (Williams *et al*. 2001). Table I displays all the different orbits of the *NEAR* spacecraft

0019-1035/02 $35.00

TABLE I
***NEAR* Mission Orbit Segments from Orbit Insertion to the Maneuver to Initiate Landing on February 12, 2001**

Segment	Start date time (UTC)	Length (days)	Orbit (km × km)	Period (days)	InclinationEros equator (°)
1	2-14-00 15:33	10.1	366 × 324	21.8	35
2	2-24-00 17:00	8.1	365 × 204	16.5	34
3	3-3-00 18:00	29.3	209 × 200	10.0	38
4	4-2-00 02:03	9.8	210 × 100	6.6	56
5	4-11-00 21:20	10.8	101 × 99	3.4	60
6	4-22-00 17:50	8.0	101 × 50	2.2	65
7	4-30-00 16:15	68.1	52 × 49	1.2	90
8	7-7-00 18:00	6.3	51 × 35	1.0	90
9	7-14-00 03:00	10.6	40 × 35	0.7	90
10	7-24-00 17:00	7.1	56 × 36	1.0	90
11	7-31-00 20:00	8.2	52 × 49	1.2	90
12	8-8-00 23:25	18.0	52 × 49	1.2	105
13	8-26-00 23:25	10.0	102 × 49	2.3	113
14	9-5-00 23:00	37.3	103 × 100	3.5	115
15	10-13-00 05:45	7.6	98 × 50	2.2	131
16	10-20-00 21:40	5.0	52 × 50	1.2	133
17	10-25-00 22:10	0.8	64 × 19	0.7	135
18	10-26-00 17:40	7.4	203 × 64	5.3	144
19	11-03-00 03:00	34.5	197 × 194	10.0	147
20	12-07-00 15:20	6.2	193 × 34	4.2	178
21	12-13-00 20:15	41.8	38 × 34	0.7	178
22	1-24-01 16:05	3.4	36 × 22	0.6	178
23	1-28-01 01:25	0.7	37 × 20	0.6	179
24	1-28-01 18:05	4.6	36 × 35	0.7	179
25	2-2-01 08:51	4.4	36 × 35	0.7	179
26	2-6-01 17:45	5.9	36 × 35	0.7	179

during its mission. The best orbit for determination of the gravity field of Eros occurred on July 14, 2000 and lasted for 10 days. This orbit was polar and circular with a radius of 35 km and provides a very strong data set for the gravity field. The tracking data from the entire remaining mission outside these ten days give only a slight improvement in the gravity field. However, all the orbits contribute to the determination of the Eros orbit around the Sun and the landmark solutions. Most orbits provide information on the rotation of Eros.

TRACKING AND LANDMARK DATA

The tracking data for *NEAR* consisted of two-way X-band Doppler tracking (∼7.2 GHz uplink and 8.4 GHz downlink) and two-way range. Although one-way Doppler (spacecraft to Deep Space Network (DSN) station) and three-way Doppler (receiving DSN station is different from transmitting) were also collected, these data were not included in the global solution because of good two-way Doppler coverage. The two-way Doppler data were processed with a sample time of 60 s. The data arcs had a typical RMS noise level 0.03 mm/s, and the RMS of the arcs varied between 0.2 and 0.5 mm/s. A total number of 317,600 Doppler measurements were processed. The Doppler data are the most important measurements for the determination of the gravity field of Eros. The range data were collected throughout the entire mission with a total of 74,180 range measurements included in the solution. The RMS accuracy of the range was less than one meter (about 2 range units or 30 cm), but due to station calibration biases the actual measurement accuracy was about 3 m for the *NEAR* spacecraft distance relative to the DSN station. The range data are critical for the determination of the Eros orbit around the Sun. The *NEAR* spacecraft was tracked mostly by the 34-m antennas of the DSN. The following station complexes were used: 14, 15, 25 (California), 34, 43, 45 (Spain), and 54 and 65 (Australia).

The other important navigation measurement in addition to the DSN tracking is the landmark observations of the surface of Eros (Owen *et al*. 2001). While the DSN tracking measures the velocity and position of the spacecraft in the line-of-sight (Earth to Eros) direction, each landmark observation from the camera provides an angle measurement in two directions of the spacecraft position relative to the Eros surface. The accuracy of the angle observations is less than one pixel of the camera. The size of the pixel for the *NEAR* camera is rectangular with dimensions of 160×90 μrad^2. This roughly amounts to a spacecraft position measurement along the spacecraft direction (alongtrack) and normal to the orbit plane of about 2–3 m for the 35-km orbit and 20–30 m for distances of 200 km. Since the Doppler measurements typically determine the radial component of the orbit the best, e.g., the *MGS* by Carranza *et al*. (2001), *Magellan* by Rappaport *et al*. (1999), and Lunar Prospector results by Carranza *et al*. (1999), the landmark tracking is an excellent complement in that it measures the other directions. The end result is an orbit that is known to several meters in all directions. The 160-μrad pixel direction is called the "line" component and is generally a measurement along the spacecraft alongtrack direction and is normal to the Sun direction. The 90-μrad pixel direction is called the "pixel" component and is generally normal to the spacecraft orbit plane and is in the direction of the Sun line.

The accuracy of the landmark data is limited by the pointing accuracy. Although the pointing knowledge of the *NEAR* spacecraft is 50 μrad, the star tracker is located on the opposite end of the spacecraft relative to the camera. Due to thermal effects and the flexing of the spacecraft deck, the attitude of the camera continuously changed by several pixels relative to the attitude specified by the star tracker. Camera attitude calibrations were performed daily by rotating the spacecraft to point the camera at a star field. The observed orientation was then compared to the star tracker orientation. With the calibrations, the pointing uncertainty was reduced to about one pixel. The ideal accuracy that one could obtain without the pointing errors is about the 1/4-pixel level given a well-defined landmark.

The landmarks chosen for the *NEAR* mission are craters that varied in size from several kilometers in radius to several meters. The actual landmark position is defined to be the center of the crater projected onto the plane tangent to the crater rim. So the landmark does not reside on the actual surface of Eros but is above the surface at a distance given by the depth of the crater. For the larger landmarks this can be significant (several

hundred meters) but for the majority of the landmarks which are smaller it is a several-meter effect. The data weight assigned to each observation depends on the size of the crater due to errors in finding the center of the crater. Larger craters have a larger uncertainty. The adopted weight σ in pixels as a function of the apparent pixel size d of the crater is

$$\sigma = [1 + (0.1d)^2]^{1/2}.$$

Figure 1 (or Fig. 3 of Owen *et al*. 2001) shows all the landmarks selected for the *NEAR* mission. Of the 1624 landmarks in the final database, 1554 were used in this study (most of the unused landmarks were only observed a few times). The landmarks or craters are grouped into different series labeled "A" to "I." The "A" series are large craters of radius 1 to 2.5 km that became visible on the north side during the early approach (Feb. 3, 2000). At this time Eros was about 40 pixels in size and at a distance of 9000 km. The "B" series began to be collected on Feb. 12, 2000

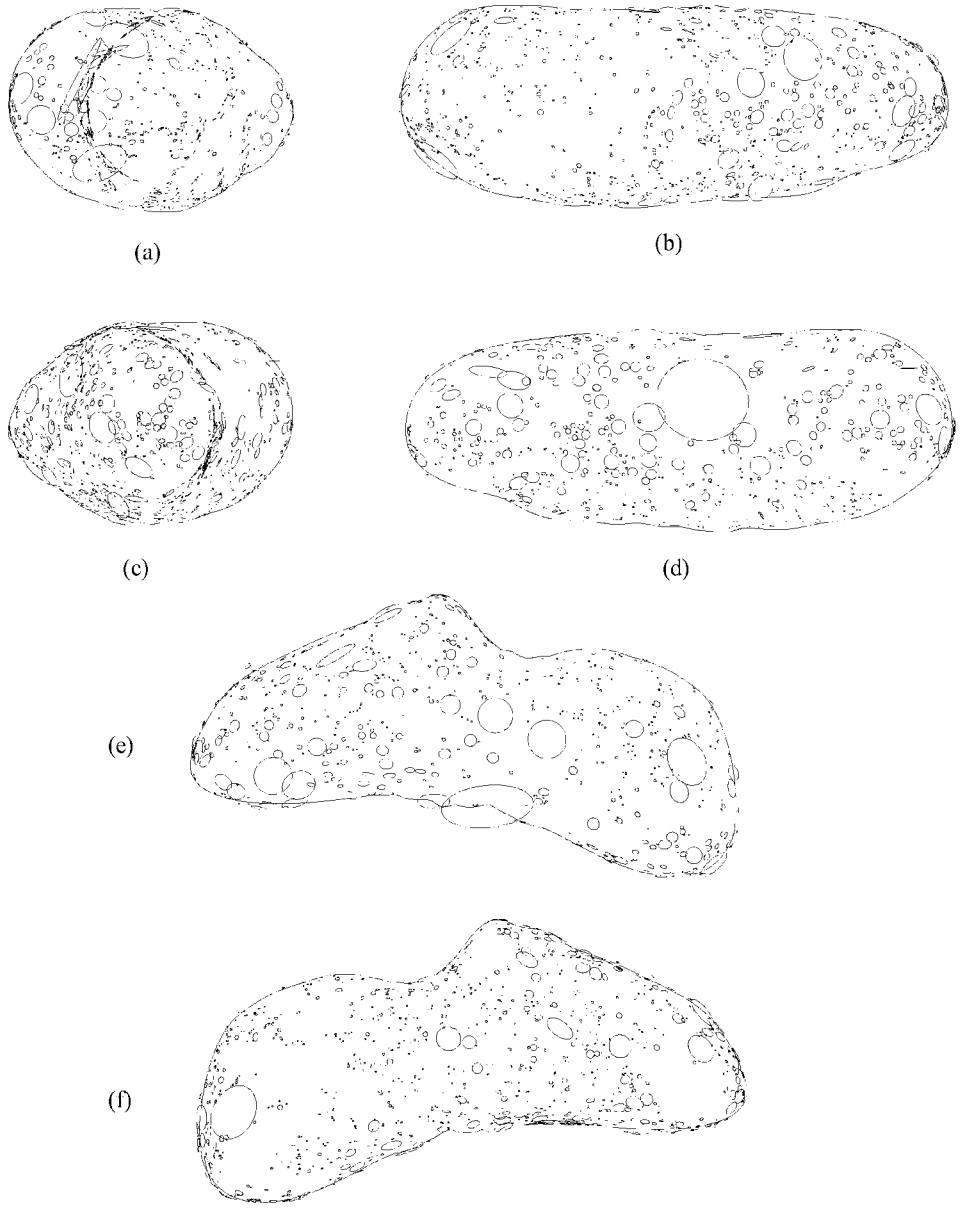

FIG. 1. The 1624 landmarks collected during the *NEAR* mission. These are plotted as seen from the (a) positive x axis, (b) positive y axis, (c) negative x axis, (d) negative y axis, (e) positive z axis (nothern hemisphere), and (f) negative z axis (southern hemisphere). This material was originally presented at the 2001 AAS/AIAA Astrodynamics Specialist Conference held July 30 to August 2, 2001, Quebec City, Quebec, Canada, and was originally published in the AAS publication, "Astrodynamics 2001", (edited by David B. Spencer, Calina C. Seybold, Arun K. Misra, Ronald J. Lisowski) American Astronautical Society (AAS) Advances in the Astronautical Sciences, Vol. 109, Part II, 2002, pp. 1075–1087 (Paper AAS 01-376, "NEAR Optical Navigation at Eros," by W. M. Owen, Jr., T. C. Wang, A. Harch, M. Bell, C. Peterson)

and are generally smaller. The "C" series were selected after orbit insertion in the equatorial region and slightly north, but mostly equatorial. Craters of all sizes are in this series. The "D" craters are smaller northern hemisphere landmarks that were chosen after the spacecraft was lowered into the 200-km orbit on March 3, 2000. The "E" series are smaller equatorial landmarks from the 200-km orbit. The "F" series are craters from the first systematic survey of the south side during the first periapse passage at 100 km on April 4 and 5, 2000. The "G" landmarks are very small northern craters from the same periapse passage. The "H" and "I" series are craters of all sizes in the far south that were not visible in April. These craters were selected from a systematic observing campaign from 100 km on June 27. There were four sets of mosaics. "H" came from the first set and "I" came from the other three.

The total number of pictures used for landmark tracking was 17,352. From these pictures, 127,593 landmark observations were generated and used in this analysis. Each landmark observation contains two measurements (one each in the "pixel" and "line" directions). Each landmark on average was observed 80 times and six of the best landmarks were observed over 500 times.

The radiometric and landmark data were divided into separate time intervals or data arcs. Over the data arc, the parameters specific to that arc, such as spacecraft state, are estimated independently for each arc. For *NEAR*, the data arcs are made as long as possible without being corrupted by nongravitational forces on the spacecraft such as thrusting. So none of the arcs contain a maneuver that was performed to change the orbit (as listed in Table I). Table I contains the start time and duration of the arcs used in this analysis with a few exceptions. The end time of an arc is typically the begin time of the next segment. The exceptions are the longer orbit segments for the 50-km orbit beginning April 30, 2000, the 100-km orbit beginning September 5, 2000, the 200-km orbit beginning November 3, and the 35-km equatorial orbit on December 13, 2000. All the other arcs are given by the begin and end times of the segment (of which the longest is 30 days on March 3 and the shortest is 19 h on October 25). In the longer segments that are exceptions, the arc size is reduced to between one and three weeks in length. Most of the arc boundaries in these cases are given by the times of momentum wheel desaturations. These occurred about once a week for the longer orbit segments mentioned above (they were not needed for any of the other orbit segments). Several of the longer arcs (2–3 weeks) included the momentum wheel desaturations within the arc. In this case, delta velocity increments are estimated to account for the maneuvers. So the most important data for the gravity (the 10-day polar, 35-km circular orbit segment starting July 14, 2000) are processed in one continuous arc. The Doppler data weight used in the filter to accentuate the gravity information was tighter for this arc at 0.05 mm/s than for all the other arcs (at 0.1 mm/s). The actual Doppler RMS data noise for the July 14 arc was 0.023 mm/s and was one of the better arcs in terms of data noise.

SOLUTION TECHNIQUE

As mentioned above, the gravity solution presented in this paper was determined using the JPL Orbit Determination Program (ODP; Moyer 1971) including the optical navigation software (Owen *et al*. 2001) and a technique that was successfully used for planetary gravity efforts of Venus (Konopliv *et al*. 1999), Mars (Yuan *et al*. 2001), and the Moon (Konopliv *et al*. 2001). The ODP estimates the spacecraft state, gravity, and other parameters using a square root information weighted least-squares filter (Bierman 1977, Lawson and Hanson 1995) in the coordinate system defined by the Earth's mean equator at the epoch of J2000. The parameters that are estimated consist of arc-dependent variables (spacecraft position, etc.) that are separately determined for each data arc and global variables (e.g., gravity coefficients and landmark positions) that are common to all data arcs. The global parameters are determined by merging only the global portion of the square root information matrix from all the arcs of the entire mission, but is equivalent to solving for the global parameters plus arc-dependent parameters of all the arcs. The technique is described by Kaula (1966) using partitioned normal matrices and was first used to analyze Earth orbiter data, and for the type of filter used in this work (square root information), the method is outlined by Ellis (1980).

Initially, we converged the data arcs by estimating only the local variables using the nominal values for the global variables. For each data arc the local variables estimated are spacecraft position and velocity at the data epoch, three solar pressure coefficients, range biases for each station pass, and a velocity increment in three directions resulting from a momentum wheel desaturation maneuver. Solving for a delta velocity was required for only a few arcs and not the critical July 14 arc.

The *NEAR* spacecraft is a simple bus spacecraft 1.7 m^2 at the base and about 2 m tall. A 1.5-m high-gain antenna is fixed to the top of the bus with four fixed solar arrays (1.2×1.8 m^2) pointing outward from the four sides of the bus. The dry mass of the spacecraft is 468 kg. The solar pressure model has two parts. The constant model is a simple bus model with a cross-sectional area of 10.3 m^2 (this model is just applied and not estimated). For the most part, the *NEAR* solar panels are Sun-pointing, so the area projected in the Sun direction is constant. To account for small changes in the solar pressure force, a small stochastic variation in three directions at about 5% of the overall force is estimated. The time constant for the stochastic solar pressure part is 1 day. It is important to minimize the a priori uncertainty of the solar pressure force being estimated because if it is too loose, it can absorb the acceleration due to the gravity field of Eros. Anything greater than 5% seems to degrade the gravity solution when looking at the correlations with topography. With a 5% a priori uncertainty, the resulting solar pressure values are at about the 5% level and cannot be absorbed by the gravity field. This model will also absorb any possible outgassing or thermal radiation.

The range data from the Earth tracking station to the *NEAR* spacecraft provide information on the Eros orbit around the Sun.

The Eros ephemeris is estimated in a separate process described below. With the new Eros ephemeris included in the estimation process, the range biases solution values are greatly reduced for every station. These biases are on the order of several meters and represent the path length calibration errors at each DSN station.

In addition to the estimated parameters, there are other different models involved in the force on the spacecraft and in the computation of the tracking and landmark observables. These include, for example, accurate Earth station position modeling to the 2- to 3-cm accuracy, ionospheric and tropospheric corrections to the Doppler and range data (based upon *in situ* GPS and weather measurements), point mass accelerations due to the Sun and planets, and relativistic time delay corrections on the radiometric observables.

The global variables determined in the solution include the pole direction and rotation rate of Eros, either the spherical harmonic gravity coefficients or ellipsoidal harmonic gravity coefficients, and the body-fixed Cartesian position of the landmarks. The orbit of Eros is also estimated with the global data set but since it is not strongly correlated with the other parameters, it can be estimated independently. Since Eros is in nearly principal axis rotation, it can be modeled mostly as a simple right ascension (α_0) and declination system (δ_0) (see Seidelmann *et al*. 2002). Each landmark position involves three parameters, α_0, δ_0, and rotation rate (W), and we estimate from the global data set the position of 1554 landmark positions for a total of 4662 landmark parameters.

Two separate solutions are generated for the complete list of global parameters. One uses spherical harmonics to model the gravity field and the other ellipsoidal harmonics. The spherical harmonic expansion to maximum degree and order N of the gravity potential is given by (see Kaula (1966) and Heiskanen and Moritz (1967))

$$U = \frac{GM}{r} \sum_{n=0}^{N} \sum_{m=0}^{n} \left(\frac{a_e}{r} \right)^n \bar{P}_{nm}(\sin\phi)[\bar{C}_{nm} \cos m\lambda + \bar{S}_{nm} \sin m\lambda]$$

where r is the radial distance from the coordinate origin, GM is the gravitational constant times the mass of Eros, n is the degree and m is the order, $\bar{P}_{nm}$ are the fully normalized associated Legendre polynominals, a_e is the reference radius of Eros (16 km for our gravity models), ϕ is the latitude, λ is the longitude, and $\bar{C}_{nm}$ and $\bar{S}_{nm}$ are the normalized gravity coefficients. The spherical harmonic model is estimated to degree and order 15 for a total of 253 parameters including the GM. The center of the coordinate system is the center of mass, so the degree one coefficients are zero. Spherical harmonics are not an ideal representation for the irregularly shaped Eros ($\sim$17 km $\times$ 6 km $\times$ 6 km) since the spherical harmonic expansion for Eros converges outside the smallest sphere that encloses the body (Heiskanen and Moritz 1967). However, all the orbits of *NEAR* except for the landing are outside the sphere, and spherical harmonics can be used as a simple straightforward investigation of the gravity and internal structure of Eros. To maintain convergence, the Bouguer gravity or differences between the measured gravity field and a gravity field assuming a constant density for Eros are displayed on a sphere of 16 km.

The second solution uses ellipsoidal harmonics. The ellipsoidal potential to maximum degree and order N is given by (Garmier and Barriot 2001)

$$U = GM \sum_{n=0}^{N} \sum_{m=0}^{2n+1} \alpha_{nm} \frac{F_{nm}(\lambda_1)}{F_{nm}(a^2 - c^2)} E_{nm}(\lambda_2) E_{nm}(\lambda_3)$$

where n and m are again the degree and order, and α_{nm} are the ellipsoidal coefficients corresponding to the spherical harmonic coefficients $\bar{C}_{nm}$ and $\bar{S}_{nm}$. For every degree there are the same number of ellipsoidal harmonics as there are spherical harmonics ($2n + 1$). The ratio involving F_{nm} is a Lamé function of the second kind and plays the same role as $(a_e/r)^n$, the attenuation factor, with distance in the spherical harmonic expansion. The variable λ_1 is a kind of radius vector, and λ_2 and λ_3 are equivalent to latitude and longitude. The semimajor axes of the ellipsoid are given by $a > b > c$. The product of E_{nm} is called a surface harmonic and is equivalent to $\bar{P}_{nm} \cos(m\lambda)$ or $\bar{P}_{nm} \sin(m\lambda)$. As with the spherical harmonics, the degree one coefficients are zero, since the coordinate system is chosen to be the center of mass.

These ellipsoidal harmonics are convergent outside the smallest ellipsoid enclosing the body and can be used to map the gravity field closer to the surface of Eros. Since Eros is much closer to the shape of a triaxial ellipsoid, fewer coefficients are needed to represent the gravity field of Eros and less noise or "aliasing" is observed in the coefficients. Whereas both the spherical harmonics and ellipsoidal harmonics give nearly the same results through roughly degree 6 or 7, the ellipsoidal solution remains much smoother to higher degrees (Garmier *et al*. 2002). However, the ellipsoidal coefficients are limited in numerical stability to about degree 12 (which is sufficient for the *NEAR* data of Eros). As mentioned above, both expansions result in the same scientific conclusions on the internal structure of Eros (Miller *et al*. 2002, Garmier *et al*. 2002). We solve for the ellipsoidal representation to degree and order 12 (167 parameters including the GM).

EROS EPHEMERIS

Eros (433) is a large near-Earth asteroid (NEA) with a semimajor axis of 1.45 AU, 0.22 eccentricity (1.13 AU perihelion distance), 10.8° inclination to the ecliptic, and a 1.76-year orbit period. The ephemeris or orbit of Eros around the Sun is very accurately determined from the ranging data to the *NEAR* spacecraft. The original range data to the *NEAR* spacecraft measure very accurately the distance to the spacecraft from the tracking station to within a few meters. Using the accurately determined *NEAR* orbits about Eros from the DSN tracking and landmark data, the range data are shifted from the *NEAR* spacecraft to the center-of-mass of Eros, also to an accuracy of several meters. These new range tracking data are then processed with the ODP

treating Eros as a spacecraft in orbit about the Sun. In addition, the telescopic images of Eros since 1964 are also processed as angle data in the ODP. Images of Eros exist as far back as 1893 but the Earth orientation data are available for the ODP with a begin date of 1964. However the range data, with a several-meter accuracy for one year, completely dominate the solution, and the optical data are not really needed. The Eros ephemeris is determined as part of an iterative procedure with the gravity field and landmarks. As a better gravity field and landmark solution is obtained, there are more accurate orbits of Eros. These orbits, in turn, provide more accurate range data to Eros and a better ephemeris of Eros. This new ephemeris is then used for the next iterative solution of the gravity field and landmarks.

The most significant perturbation on the Eros orbit during the *NEAR* mission other than the Sun is a 0.416-AU flyby of the asteroid Vesta on July 13, 2000. This allows for an estimate of the mass of Vesta. There are no other major perturbations on Eros. The next largest effects are encounters by Sappho (80) at 0.17 AU, Flora (8) at 0.39 AU, Desiderata (344) at 0.51 AU, and Bruchsalia (455) at 0.40 AU. All these effects are too small to yield a mass estimate.

Figure 2 shows the residual range data to Eros when the Vesta perturbation is not included, and the fit with the mass of Vesta estimated. The only other parameters estimated other than the mass of Vesta is the initial position and velocity of Eros. However, the perturbations on Eros from the Sun and planets are included in the force model. Table II shows the different estimates of the mass of Vesta (from Table 4 in Krasinsky *et al.* 2001), including the more recent estimate from the JPL planetary ephemeris effort (Standish, Jet Propulsion Laboratory internal document IOM 312.F-01-006, 2001), and the result of this effort. Our estimate is consistent with most of the determined values of Vesta. There are higher values of Vesta ($\sim$20.0 km^3/s^2) but our RMS of the range residuals shows an increase of 41% to 1.9 m from the best-fit RMS of 1.3 m in Fig. 2b when the Vesta mass is fixed to this higher value. So these higher values are not consistent with the Eros data. If the mass is fixed to the lower value of 17.8 km^3/s^2 of the JPL planetary ephemeris effort, then the RMS only increases by a modest 2.7%, and so we consider the lower values in Table II to be consistent with our results. The error we give is about 2.5 times the formal error of 0.16 to give a more realistic error value of 0.4. The range residuals in Fig. 2b are the result of both orbit error and DSN range calibrations at the station. The signature in the residuals at 200 to 300 days past the epoch of the data is mostly due to spacecraft orbit error. At this time the *NEAR* orbit at Eros is larger and hence has a larger orbit error because the landmark tracking is not as accurate at the higher orbits. This is consistent with the orbit errors we see from different orbit solutions as discussed in the landmark results. The mass estimate of Vesta does not change if range biases are solved for each DSN range pass. In this case the RMS of the residuals reduces to about 20 cm.

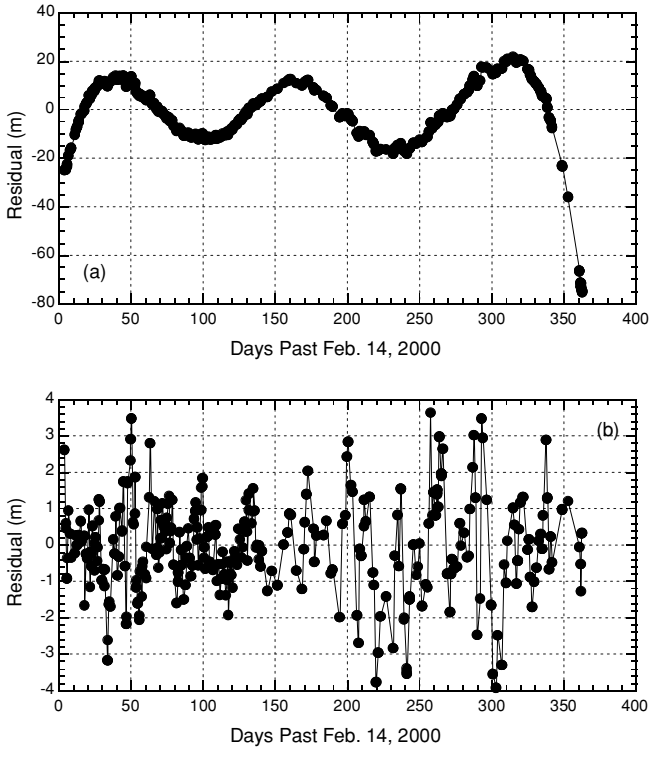

FIG. 2. Range residuals to Eros for (a) zero Vesta mass, and (b) the mass of Vesta estimated.

TABLE II
Mass Estimates of Vesta

Vesta mass (km^3/s^2)	Vesta mass 10^{-12} Solar Mass	Perturbed body	Reference
18.3	138	(197) Arete	Rapaport and Viateua (1998)
21.0	158	(197) Arete	Hilton *et al.* (1996)
20.2	152	(1) Ceres	Hilton *et al.* (1996)
17.8	134	22 asteroids	Kuznetsov (1999)
18.0	136	26 asteroids	Michalak (2000)
19.4	146	4 asteroids	Krasinsky *et al.* (2001)
17.8 ± 0.2	134 ± 1.5	Mars	Standish (JPL planetary ephemeris 2001)
18.2 ± 0.4	137 ± 3.0	Eros	This paper

Additional information is visible in Fig. 2b. Prior to the large orbit errors that dominate beginning 220 days after the epoch, a monthly oscillation is visible in the range residuals. The amplitude is about 1.5 m. This is due to the motion of the Earth about the barycenter of the Earth–Moon system. This allows us to put constraints on the Earth–Moon mass ratio. The solution for the Eros orbit and Vesta mass used the JPL planetary ephemeris DE403. DE403 uses a mass ratio of 81.300585. The latest constraint on the mass ratio is from the Lunar Laser Ranging (LLR) and Lunar Prospector results (Konopliv *et al.* 1998) where the value is 81.300566 ± 0.000020. The result from Fig. 2b is nearly the same, except the uncertainty can be reduced. The range data to Eros results in an Earth–Moon mass ratio of 81.300570 ± 0.000005 and an improved lunar *GM* value of 4902.8000 ± 0.0003 km^3/s^2.

LANDMARK RESULTS

As the result of the landmark observations, the orbits of *NEAR* are very well determined. The landmarks are very important for the higher altitude orbits. For the initial 350-km circular orbit of *NEAR*, for example, the landmark tracking lowers the overall orbit error to hundreds of meters or less, whereas the orbit error with radiometric tracking alone is about 20 km. The orbit error for the close orbits (35 km) is several meters in all three directions and for the most part can be obtained with sufficient radiometric tracking alone. However, the landmark tracking reduces the time required to redetermine the spacecraft position after a maneuver. These orbit error results were determined by differencing orbits where the only change in the solution procedure is that one contains only radiometric tracking and the other includes landmark tracking.

To quantify the orbit error with landmark tracking, orbits determined with the ODP (this paper or Radio Science Team orbits) were differenced with those determined by the Navigation Team using the PCODP software. Both solutions use the radiometric and landmark data. However, both procedures are very independent with different data arc intervals and spacecraft models, and the PCODP used a subset of the landmarks. These differences together with the differences of the orbits determined by the NLR Team have been included in the PDS archive for *NEAR*. The orbit differences are computed not as an RMS but as an average of the absolute value of the difference. The NLR orbits are determined using radiometric data and NLR altimeter measurements, and are the result of a joint gravity and shape estimation. The NLR orbit set begins with the 200-km orbit on March 3, 2000 with the collection of altimetry.

Figure 3 displays the orbit differences in all three components (radial, transverse, and normal to the orbit) between Radio Science and the other two sets. The orbit differences for the higher 200-km orbits are tens of meters for the landmark tracking orbits and hundreds of meters for the NLR orbits, which do not contain landmark tracking. The sudden decrease in solution differences in Fig. 3 occurs at the transition from higher to lower altitude orbits. The initial 350-km orbit (Feb. 14–24) differences for the landmark orbits are several hundred meters and are off the scale in Fig. 3a. For the lower orbits, the landmark orbit solutions (ODP, PCODP) agree to mostly better than 5 m. This most likely is near the true orbit uncertainty for the 35-km orbit for the Radio Science or Navigation orbit solutions. Other results also support orbit error at this level. The range residuals for the ephemeris of Eros (Fig. 2) suggest that the Radio Science orbit error in the Earth line-of-sight direction is less than 2 m. If orbit errors were greater, we would see a larger scatter in the Eros range residuals of Fig. 2 since the Eros range measurements must be first corrected for *NEAR* position relative to the Eros center-of-mass. In addition, the typical total landmark statistical error in position is less than 5 m, and the resulting RMS of landmark image residuals is typically less than one pixel. No systematic errors are apparent in the optical data and are not likely hidden since no pointing corrections or biases are estimated

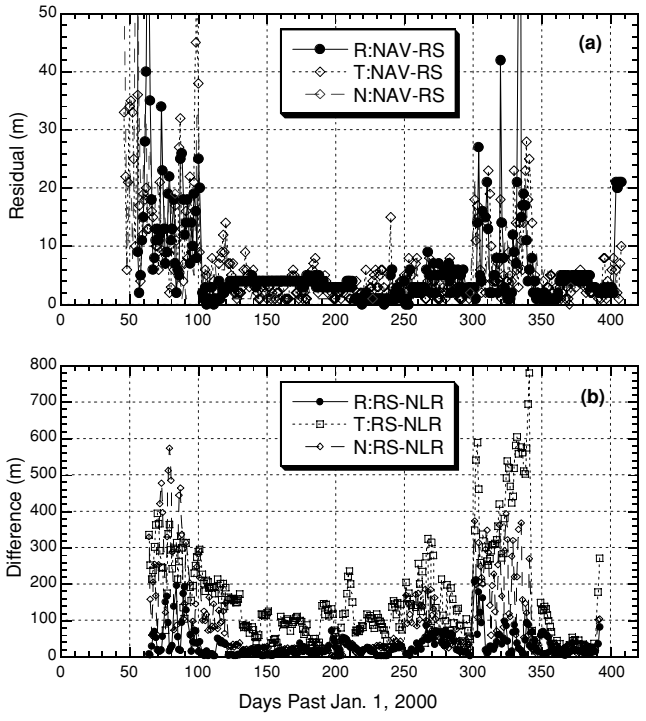

FIG. 3. Average orbit differences between (a) Radio Science and Navigation, and (b) Radio Science and NLR.

with the optical data. When optical data are eliminated from the 35-km orbit solution, the resulting radiometric-only solution differs from the solution with optical by an RMS of 0.6 m radially, 4.1 m alongtrack, and 0.8 m crosstrack. This indicates the consistency of the radiometric data together with the landmark tracking.

The positions of the smaller craters or landmarks of the global solution are determined to an accuracy of about 2 m for all three body-fixed directions on the surface of Eros. The larger landmarks have uncertainties of tens of meters and, in several cases, up to 200 m.

Next we compare the landmark positions with the 180th degree and order Eros spherical harmonic shape model derived by the NLR Team (Zuber *et al*. 2000). The x, y, and z Eros body-fixed position of each landmark is estimated in the global solution process with the resulting uncertainty being about 2–3 m in each direction. The corresponding latitude, longitude, and radius are then computed for each landmark. Using the latitude and longitude of the landmark, the radius from the NLR shape model is computed. The radius values from the landmarks and NLR shape model are then differenced and displayed in Fig. 4.

Figure 4a shows the original differences. We suspected that the coordinate systems of this global solution might be different from the NLR coordinate system. This is due to different pole and rotation values used and to orbit corrections applied in the shape model crossover analysis. The radial differences were again calculated after rotating the body-fixed coordinate

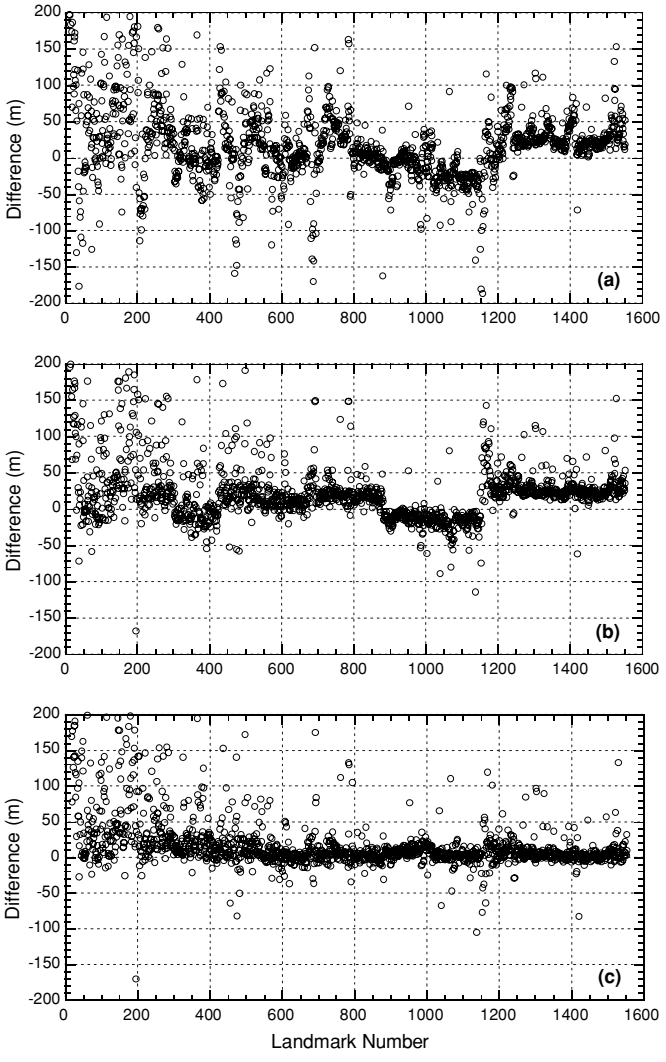

FIG. 4. Differences of landmark position solution and 180th degree NLR shape model of Zuber *et al.* (2000) for (a) original coordinate system of NLR shape model, (b) NLR shape model rotated by $+0.155^\circ$ about the z axis, and (c) NLR shape model rotated about the z axis and shifted down the z axis by 19 m (i.e., in the negative direction).

system of the NLR shape model by $+0.155^\circ$ about the z axis (i.e., features are shifted to the left in longitude in the map of the shape model in the new coordinate system). The results are displayed in Fig. 4b. Much of the noise and structure was removed. Next the NLR shape model was rotated as above and then shifted along the negative z axis by 19 m and displayed in Fig. 4c. This was very successful in laying the residuals flat. The discontinuity in Fig. 4b at landmark numbers 880 and 1150 correspond to "G" craters being located in the northern hemisphere and then "H" and "I" craters in the south.

The landmark and NLR shape differences are very sensitive to shifts in the z component of the shape model but are not as sensitive to translations in the x and y directions. So the landmarks can be used to constrain the z height difference between the center-of-mass and center-of-figure coordinate systems. The location of the center of figure of the shape model before the translation of the z axis is -13, 0, and $+32$ m in the x, y, and z direction, respectively. The shape center-of-figure is defined to be the center-of-mass of the shape's gravity assuming a constant density, and it is determined by numerical integration over the volume. With the translation of the shape z axis, the new location of the z component of the center-of-figure offset is $+13$ m. So the center-of-mass and center-of figure offset has reduced significantly and indicates a more uniform Eros in the z direction. With the overall length of Eros in the x direction of 34 km and z length of 11 km, this indicates long-wavelength density variations of less than 1%.

In Fig. 4, the landmarks are listed in order of selection. Again, each landmark position is not on the true surface of Eros. It is the center of the crater projected upward to the rim of the crater. So it is above the surface by an amount equal to the depth of the crater. The initial landmarks were larger, and Fig. 4 shows the larger depth for these initial craters. For the smaller craters beyond number 600, the depths are smaller and mostly below 10 m and as low as 1 or 2 m. Negative differences and some positive differences are due to either errors in the landmark or possible gaps in the NLR data where results are interpolated. The RMS of the differences is 5.6 m for the smaller landmarks (1250 to 1550) with outliers greater than 20 m deleted. This result is much better than any shape model from the Navigation Team (Yeomans *et al.* 2000, Miller *et al.* 2002, Bordi *et al.* 2000) or those by the main author (estimated to degree 120). These models have very accurate long-wavelength information but poor short-wavelength information. The NLR model does very well in both the long- and short-wavelength features as shown by the comparison with the landmark solutions.

GRAVITY RESULTS

The gravity field of Eros was modeled with both spherical harmonics and ellipsoidal harmonics. Although spherical harmonics are not an ideal representation for the irregularly shaped Eros, they still can be used to evaluate the uniformity of Eros. In this paper we mostly discuss the spherical harmonic results.

TABLE III
Gravity and Gravity from Shape Spherical Harmonic Correlations

	Correlations	
Harmonic degree	This paper	Miller *et al.* (2002)
2	1.00000	0.99999
3	0.99973	0.99961
4	1.00000	0.99999
5	0.99987	0.99972
6	0.99981	0.99967
7	0.9994	0.9983
8	0.9940	0.9916
9	0.974	0.928
10	0.686	0.523

Note. The shape model used in this paper is from the NLR Team, Zuber *et al.* (2000).

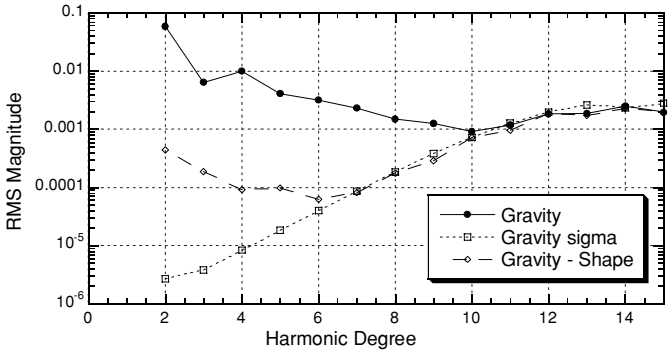

FIG. 5. RMS magnitude spectrum of the gravity and gravity uncertainty. Also included is the RMS difference of the gravity and gravity from shape assuming constant density. The NLR shape model is used (Zuber *et al.* 2000).

The ellipsoidal harmonic conclusions are nearly identical, and the ellipsoidal solution generated by this work has been presented previously (Garmier *et al*. 2002). The NLR shape model of Zuber *et al*. (2000) is used to display the results in this section, but the Navigation and Radio Science shape models give nearly identical results.

One way to compare different gravity and topography solutions is to look at the correlations between the coefficients. The correlations are dominated by the ellipsoidal shape of the gravity and topography, and so are nearly equal to 1. However, small changes in the correlations indicate which solutions match more closely. The correlations for this solution are ever so slightly larger than the previous results (Miller *et al*. 2002), which used a radiometric-only gravity solution and the Navigation Team shape model. The correlations through degree 10 are shown in Table III for this gravity solution (radiometric plus landmark tracking) and the NLR shape model, and the previous results. From Table III, one notes that the correlation between gravity and shape dramatically reduces at degree 10. This is because the gravity field is determined to roughly degree and order 10.

Figure 5 shows the RMS magnitude spectrum of the gravity field with both the RMS of the coefficients and the RMS of coefficient uncertainty. The a priori constraint in the gravity field (0.005 for $n = 11$ to 15) is visible in the higher RMS of the uncertainty and gravity for $n > 10$. The uncertainty in the coefficients or noise matches the coefficient magnitude or signal at degree 10. So, the gravity field of Eros is determined to about degree 10 or about a 5-km half-wavelength resolution. However, the amplitude of the difference in the coefficients is much smaller, and the differences between the gravity and shape can be investigated only to degree 7. This is demonstrated in Fig. 5 by the difference of the gravity solution with the gravity from shape assuming a constant density. Note that the uncertainty and differences in Fig. 5 are again only slightly improved over the previous results of Miller *et al*. (2002). While the center-of-mass and center-of-figure offsets indicate very small large-scale changes in density (<1%), the differences between the coefficients of the gravity and shape are larger at 1–5% of the gravity amplitude.

The next task is to investigate the differences in gravity and gravity from shape in the spatial domain. The Bouguer gravity is defined as the difference of the radial component of the gravity and gravity from shape assuming a constant density. The accelerations are determined on a sphere of 16 km. With *NEAR* being in a circular orbit about Eros, the gravity of the ends of the asteroid is much better determined than that of the center of the asteroid. The uncertainty in the gravity when mapped on the 16-km sphere is roughly uniform (less than 1 mgal), and the gravity of the ends is more visible than the rest of the asteroid. The previous Bouguer results of Miller *et al*. (2002) had maximum and minimum values of 1.75 and −3.86 mgal, respectively. The new results as shown in Fig. 6 are nearly the same and

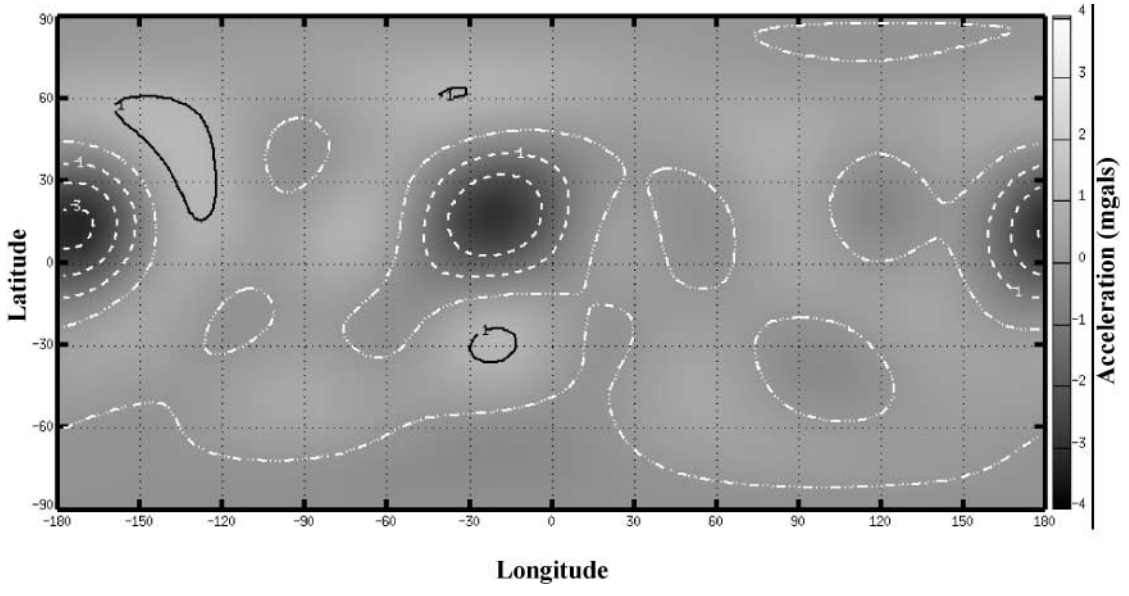

FIG. 6. Eros Bouguer radial acceleration map. Differences between gravity and topography are shown on a sphere of 16 km.

show the acceleration differences for the gravity and shape for spherical harmonics from degree 2 to 6. The range or maximum and minimum have slightly reduced to 1.26 and −3.28 mgal, respectively. The locations of the features are unchanged. We still have negative Bouguer anomalies located at the ends of Eros (−3.28 mgal for the negative x-axis and −2.98 mgal in the positive x-axis direction) and slightly shifted to the northern hemisphere (Miller *et al*. 2002). The amplitude of the Bouguer gravity at the ends of the asteroid is about 1% of the gravity amplitude (without the *GM* and for degrees 2 to 6).

The negative Bouguer values indicate that the density of the asteroid ends is slightly less than the rest of the asteroid. A regolith cannot account for the entire negative anomaly. For instance, a 100-m regolith with a density of 2.0 gm/cm^3 (versus the mean 2.6 gm/cm^3) gives a Bouguer value of −1.0 mgal at the negative x-axis end and −0.4 mgal at the positive x-axis end. We would need about three times this effect to account for what is observed. The lower density ends may also be the result of an increase in density near the center of the asteroid. The full Bouguer signature can be accounted for by an increase in density of 5% for 20% of the asteroid volume near the center of the asteroid or equivalently a 10% increase for 10% of the volume. At the center of the asteroid is the Psyche crater and Himeros depression. The small positive anomalies noted in the Bouger gravity in the ellipsoidal results of Garmier *et al*. (2002) lead to the suggestion of possible compression from impact. As with the spectral differences in Fig. 5, the density contrasts suggested by the Bouguer analysis are larger than the center-of-mass and center-of-figure offsets. Whatever variations we see need to average to nearly 0 on the global scale such as a regolith or radial decrease in density from the asteroid center. However, the comparison of the gravity and shape models still indicates (but do not prove) a fairly uniform Eros.

Also determined in the global solution is the *GM* and rotation of the asteroid Eros. These values are listed in Table IV along with a realistic uncertainty. The uncertainty is about 5 times the formal uncertainty we get in the global solution. The factor of 5 scaling was determined by looking at subset solutions for the pole and rotation. The pole and rotation rate are best determined by the 35-km circular equatorial orbits near the end of the mission. These orbits result in an uncertainty of 4–5 times lower for the pole and about 2 times less for the rotation rate. It is expected that the solar gravity gradient torque will cause a nine-month oscillation in the pole of about 0.01° (Miller *et al*. 2002). However, we have less than two months of the data sensitive to the pole, and it is difficult to detect this pole motion. In the data that was not as sensitive to the pole, long-term motion of about five months from minimum to maximum and 0.01° is visible in the pole right ascension and declination, but this motion is near the uncertainty in the pole. So detection of the solar gravity gradient torque is not conclusive.

TABLE IV
Eros *GM* and Rotation Solution

Parameter	Solution
GM	$(4.4627 \pm 0.0001) \times 10^{-4}$ km^3/s^2
Pole right ascension	$11.363 \pm 0.001°$
Pole declination	$17.232 \pm 0.001°$
Rotation rate	$1639.38928 \pm 0.00001°$/day
Prime meridian (fixed)	326.08

ACKNOWLEDGMENTS

Other members of the JPL navigation team provided files, tables, and information needed for this effort. They include T. C. Wang, B. G. Williams, P. G. Antreasian, and J. J. Bordi. Also A. Chamberlin of the small body ephemeris group helped with the conversion of the Eros ephemeris files and E. M. Standish provided information on the solution for the Vesta mass and the Earth–Moon mass ratio. The research described in this paper was carried out at the Jet Propulsion Laboratory, California Institute of Technology, under contract with the National Aeronautics and Space Administration.

REFERENCES

Bierman, G. J. 1977. *Factorization Methods for Discrete Sequential Estimation.* Academic Press, New York.

Bordi, J. J., J. K. Miller, B. G. Williams, R. S. Nerem, and F. J. Pelletier 2000. The impact of altimeter range observations on NEAR navigation. In *A Collection of AIAA/AAS Astrodynamics Specialist Conference Technical Papers: Denver, CO August 14–17, 2000,* pp. 486–496. AIAA, Reston.

Carranza, E., A. S. Konopliv, and M. Ryne 1999. Lunar Prospector orbit determination uncertainties using the high resolution lunar gravity models. In *Advances in the Astronautical Sciences* (K. C. Howell, F. R. Hoots, B. Kaufman, and K. T. Alfriend, Eds.), Vol. 103, pp. 381–400. Univelt, San Diego.

Carranza, E., D. N. Yuan, and A. S. Konopliv 2001. Mars Global Surveyor orbit determination uncertainties using high resolution Mars gravity models. In *Advances in the Astronautical Sciences* (D. B. Spencer, C. C. Seybold, A. K. Misra, and R. J. Lisowski, Eds.), Vol. 109, pp. 1633–1650. Univelt, San Diego.

Ellis, J. 1980. Large scale state estimation algorithms for DSN tracking station location determination. *J. Astronaut. Sci.* **28**, 15–30.

Garmier, R., and J. P. Barriot 2001. Ellipsoidal harmonic expansions of the gravitational potential: Theory and Application. *Celest. Mech. Dynam. Astron.* **79**, 235–275.

Garmier, R., J. P. Barriot, A. S. Konopliv, and D. K. Yeomans 2002. Modeling of the Eros gravity field as an ellipsoidal harmonic expansion from the NEAR Doppler tracking data. *Geophys. Res. Lett.* **29**, 721–723.

Heiskanen, W. A., and H. Moritz 1967. *Physical Geodesy.* W. H. Freeman, San Francisco, CA.

Hilton, J. L., P. K. Seidelman, and J. Middour 1996. Prospects for determining asteroid masses. *Astron. J.* **112**, 2319–2329.

Kaula, W. M. 1966. *Theory of Satellite Geodesy*. Blaisdell, Waltham, MA.

Konopliv, A. S., S. W. Asmar, E. Carranza, W. L. Sjogren, and D. N. Yuan 2001. Recent gravity models as a result of the lunar prospector mission. *Icarus* **150**, 1–18.

Konopliv, A. S., W. B. Banerdt, and W. L. Sjogren 1999. Venus gravity: 180th degree and order model. *Icarus* **139**, 3–18.

Konopliv, A. S., A. B. Binder, L. L. Hood, A. B. Kucinskas, W. L. Sjogren, and J. G. Williams 1998. Improved gravity field of the Moon from lunar prospector. *Science* **281**, 1476–1480.

Krasinsky, G. A., E. V. Pitjeva, M. V. Vasilyev, and E. I. Yagudina 2001. Estimating masses of asteroids. *Commun. Inst. Appl. Astron.* **139**, St. Petersburg, Russia.

Kuznetsov, V. 1999. On determination of masses of the largest asteroids. *Tr. Inst. Appl. Astron.* **4**, 117–127.

Lawson, C. L., and R. J. Hanson 1995. *Solving Least Squares Problems*, SIAM Classics in Applied Mathematics Vol. 15. SIAM, Philadelphia.

Michalak, G. 2000. Determination of asteroid masses, I. (1) Ceres, (2) Pallas, and (4) Vesta. *Astron. Astrophys.* **360**, 363–374.

Miller, J. K., A. S. Konopliv, P. G. Antreasian, J. J. Bordi, S. Chesley, C. E. Helfrich, W. M. Owen, D. J. Scheeres, T. C. Wang, B. G. Williams, and D. K. Yeomans 2002. Determination of shape, gravity, and rotational state of Asteroid 433 Eros. *Icarus* **155**, 3–17.

Moyer, T. D. 1971. Mathematical formulation of the double-precision orbit determination program (DPODP), JPL Technical Report 32-1527. Jet Propulsion Laboratory, California Institute of Technology, Pasadena, CA.

Owen, W. M., Jr., T. C. Wang, A. Harch, M. Bell, and C. Peterson 2001. NEAR optical navigation at Eros. In *Advances in the Astronautical Sciences* (D. B. Spencer, C. C. Seybold, A. K. Misra, and R. J. Lisowski, Eds.), Vol. 109, pp. 1075–1090. Univelt, San Diego.

Rapaport, M., and B. Viateau 1998. Determination of masses of asteroids. Recent developments and projects. In *Proceedings of The Fourth International Workshop on Positional Astronomy and Celestial Mechanics* (A. Lopes Garcia, L. I. Yagudin, M. J. Uso, A. Cordero Barbero, E. I. Yagudina, and J. A. Morano, Eds.), pp. 237–244. Universitat de Valencia, Valencia.

Rappaport, N. J., A. S. Konopliv, A. B. Kucinskas, and P. G. Ford 1999. An improved 360 degree and order model of the Venus topography. *Icarus* **139**, 19–30.

Seidelmann, P. K.,V. K. Abalakin, M. Bursa, M. E. Davies, C. de Bergh, J. H. Lieske, J. Oberst, J. L. Simon, E. M. Standish, P. Stooke, and P. C. Thomas 2002. Report of the IAU/IAG Working Group on cartographic coordinates and rotational elements of the planets and satellites: 2000. *Celest. Mech. Dynam. Astron.* **82**, 83–110.

Williams, B. G., P. G. Antreasian, J. J. Bordi, E. Carranza, S. R. Chesley, C. E. Helfrich, J. K. Miller, W. M. Owen, and T. C. Wang 2001. Navigation for NEAR Shoemaker: The first spacecraft to orbit an asteroid. In *Advances in the Astronautical Sciences* (D. B. Spencer, C. C. Seybold, A. K. Misra, and R. J. Lisowski, Eds.), Vol. 109, pp. 973–988. Univelt, San Diego.

Yeomans, D. K., P. G. Antreasian, J. P. Barriot, S. R. Chesley, D. W. Dunham, R. W. Farquhar, J. D. Giorgini, C. E. Helfrich, A. S. Konopliv, J. V. McAdams, J. K. Miller, W. M. Owen, Jr., D. J. Scheeres, P. C. Thomas, J. Veverka, and B. G. Williams 2000. Radio science results during the NEAR-Shoemaker spacecraft rendezvous with Eros. *Science* **289**, 2085–2088.

Yuan, D. N., W. L. Sjogren, A. S. Konopliv, and A. B. Kucinskas 2001. Gravity field of Mars: A 75th degree and order model. *J. Geophys. Res.* **106**, 23,377–23,401.

Zuber, M. T., D. E. Smith, A. F. Cheng, J. B. Garvin, O. Aharonson, T. D. Cole, P. J. Dunn, Y. Guo, F. G. Lemoine, G. A. Neumann, D. D. Rowlands, and M. H. Torrence 2000. The shape of 433 Eros from the NEAR-Shoemaker Laser Rangefinder. *Science* **289**, 2097–2101.